IEEE Open Journal of
Antennas and Propagation

Received 6 August 2020; revised 3 September 2020; accepted 7 September 2020. Date of publication 15 September 2020; date of current version 6 October 2020.

Digital Object Identifier 10.1109/OJAP.2020.3024276

Microwave Detection of Brain Injuries by Means of a Hybrid Imaging Method

ALESSANDRO FEDELI [1] (Member, IEEE), CLAUDIO ESTATICO [2], MATTEO PASTORINO [1] (Fellow, IEEE), AND ANDREA RANDAZZO [1] (Senior Member, IEEE)

[1]Department of Electrical, Electronic, Telecommunications Engineering and Naval Architecture (DITEN), University of Genoa, 16145 Genoa, Italy

[2]Department of Mathematics (DIMA), University of Genoa, 16146 Genoa, Italy

CORRESPONDING AUTHOR: A. RANDAZZO (e-mail: andrea.randazzo@unige.it)

ABSTRACT Brain injuries represent a critical situation, where both detection and monitoring should be quick and accurate at the same time. Microwave techniques are thus gaining attention in the diagnostic process of these diseases. However, the detection of inhomogeneities and variations inside the human brain by using electromagnetic fields at microwave frequencies is a very challenging inverse problem. An innovative hybrid microwave imaging method is introduced in this contribution, which combines the benefits of a fast qualitative processing technique with an accurate tomographic reconstruction of the dielectric properties of the human head. This method has been successfully applied to obtain microwave images from both synthetic data and laboratory measurements. Numerical simulations involve three-dimensional realistic models of stroke-affected heads, whereas simplified cylindrical phantoms have been exploited for the experimental validation of the approach. In both conditions, the proposed technique yields promising results, which may be considered a preliminary step towards the realization of a clinical imaging prototype.

INDEX TERMS Microwave imaging, inverse scattering, brain stroke, hybrid methods.

I. INTRODUCTION

ONE OF the most critical diagnostic situations, when proper therapeutic decisions should be taken as rapidly as possible, is related to patients affected by brain injuries. An example is given by stroke [1], a well-known disease whose sudden occurrence affects a significant percentage of the elder population worldwide and which may lead to death or permanent disabilities [2].

The diagnosis of brain injuries customarily relies on computerized tomography (CT) and magnetic resonance imaging (MRI). However, such imaging devices cannot be used on-site for a pre-hospital investigation. To overcome this problem, several approaches are under test. Microwave techniques, although not yet included in common clinical practice, are now listed among the promising pre-hospital technologies to aid stroke diagnosis [3], [4].

Indeed, the microwave detection of brain injuries and strokes has known a relevant development in the last years, leading to several systems and algorithms [5], [6]. The advent of wearable electromagnetic applications has further pushed the research towards this direction, with an intensive study about flexible and biomatched radiating devices to be employed in portable systems [7]–[10].

Besides classification-based methods [11], [12], the scientific research about microwave imaging for brain injuries detection and monitoring usually follows two distinct paths. One of these is represented by qualitative approaches, whose scope is to produce an image that spots the stroke location, without information about its dielectric characteristics [13]–[16]. Benefits of these strategies include speed, reduced computational burden, and robustness versus noise. Nevertheless, having a pointwise indication about the material of the inhomogeneity inside brain may represent a concrete aid in the diagnosis of these pathologies. This is the application field of quantitative imaging techniques [17]–[21]. The progress in this area is continuous, and some recent advances have been obtained by adopting deep-learning-aware inverse scattering methods [22]–[26]. However, the quantitative retrieval of the head properties by

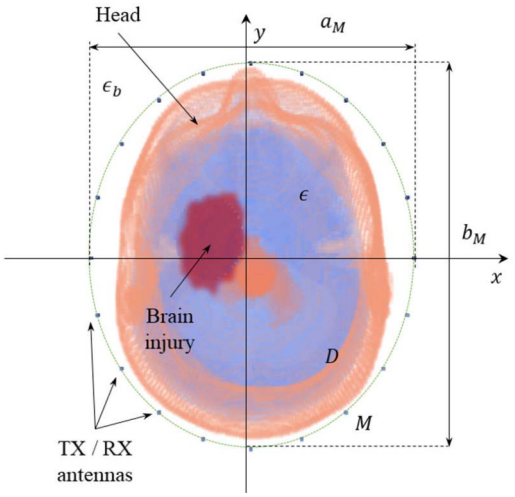

FIGURE 1. Configuration of the brain injury characterization problem. A set of antennas is placed on a measurement line around patient's head.

using microwave radiation still constitutes a very challenging inverse problem.

In this framework, good results have been also obtained in tomographic configurations by adopting regularization methodologies developed outside the conventional setting of Hilbert spaces [27], [28]. However, even in the best-performing variable-exponent Lebesgue-space algorithm [28], a fully adaptive definition of the exponent map (which is a function of the position inside the investigation domain) was not exploited from the first Newton iterations due to the absence of a-priori information about the scene under investigation.

The above considerations have led to the development of the hybrid inverse-scattering technique proposed in this article. This approach aims at combining the benefits of a qualitative method, based on a synthetic-aperture focusing technique, with a nonlinear variable-exponent inversion. In particular, the map retrieved by the qualitative technique is adopted inside the inexact-Newton scheme to define the exponent function. To the best of our knowledge, this is the first time that a hybrid qualitative-quantitative nonlinear inversion method of this kind is proposed for microwave detection of brain injuries. Its validation has been done against simulated data, thanks to the definition of stroke-affected three-dimensional head phantoms, as well as with a preliminary experimental configuration involving a system prototype and liquid-filled cylindrical targets.

The paper has the following structure. In Section II, the proposed hybrid imaging method is presented, starting from the statement of the inverse problem. Sections III and IV discuss numerical and experimental results, respectively. At the end, conclusions are outlined in Section V.

II. METHODS AND PROCEDURES

Let us start by considering a tomographic configuration, where patient's head is illuminated in turn by a set of S antennas placed around it, as sketched in Fig. 1. In this way, a multiview arrangement is created. Radiated electric fields are assumed to be z-polarized and without components on the xy plane (i.e., transverse-magnetic) inside the inversion procedure, to retain a scalar and two-dimensional problem formulation [5]. A horizontal cross section of patient's head is enclosed in a two-dimensional investigation domain D of arbitrary shape lying on the xy plane, where $\mathbf{r}_t = x\hat{\mathbf{x}} + y\hat{\mathbf{y}}$ indicates the position vector. For each position of the source antenna $\mathbf{r}_t^s$ $(s = 1, \ldots, S)$, the z component of the electric field is collected in a measurement domain M_s $(s = 1, \ldots, S)$ which is an elliptic line at the same height of the source with axes length a_M and b_M, respectively. Nonmagnetic materials are assumed, that is, magnetic permeability is $\mu = \mu_0 \simeq 4\pi \times 10^{-7}$ H/m everywhere. A frequency-domain formulation is assumed here with an $e^{j\omega t}$ time dependence of field quantities (not shown for brevity), $\omega \in B$ being the angular frequency that lies in band B.

A. STROKE IMAGING AS A NONLINEAR INVERSE PROBLEM

In a stroke imaging application, the aim is to reconstruct the distribution of dielectric properties inside the head, in order to identify and monitor the pathology. To this end, two different conditions are considered. The first one is characterized by a reference distribution of the dielectric permittivity $\epsilon_{t0}(\mathbf{r}_t, \omega)$, which is assumed to be known (e.g., by previous measurements, eventually obtained with other imaging modalities like MRI), whereas the second one is represented by the actual pathologic condition, characterized by dielectric permittivity $\epsilon_{t1}(\mathbf{r}_t, \omega)$. These two situations correspond to z-components of electric fields $E_{s,t0}(\mathbf{r}_t, \omega)$ and $E_{s,t1}(\mathbf{r}_t, \omega)$, respectively, with $s = 1, \ldots, S$, $\mathbf{r}_t \in \mathbb{R}^2$. In each case, a set of S differential equations relates the electric field to the dielectric properties of the scene, i.e.,

$$\left[\nabla^2 + \omega^2 \mu_0 \epsilon_{ti}(\mathbf{r}_t, \omega)\right] E_{s,ti}(\mathbf{r}_t, \omega) = j\omega\mu_0 J_s(\mathbf{r}_t, \omega), \quad (1)$$

where $i = 0, 1$ and $s = 1, \ldots, S$, $J_s(\mathbf{r}_t, \omega)$ being the z-component of the current density that generates the sth incident radiation (assumed the same in both cases). In order to retrieve the dielectric variation between these two situations, a contrast function $\tau(\mathbf{r}_t, \omega) = [\epsilon_{t1}(\mathbf{r}_t, \omega) - \epsilon_{t0}(\mathbf{r}_t, \omega)]/\epsilon_b(\omega)$ and a difference field, $\Delta E_s(\mathbf{r}_t, \omega) = E_{s,t1}(\mathbf{r}_t, \omega) - E_{s,t0}(\mathbf{r}_t, \omega)$, $s = 1, \ldots, S$, are defined, where $\epsilon_b(\omega) = \epsilon_0 \epsilon_{r,b}(\omega)$ is the dielectric permittivity of the considered background medium.

Under these conditions, the electromagnetic problem is summarized by the following system of equations:

$$\left[\nabla^2 + \omega^2 \mu_0 \epsilon_{t0}(\mathbf{r}_t, \omega)\right] \begin{bmatrix} \Delta E_1(\mathbf{r}_t, \omega) \\ \vdots \\ \Delta E_S(\mathbf{r}_t, \omega) \end{bmatrix} = j\omega\mu_0 \begin{bmatrix} J_1^\tau(\mathbf{r}_t, \omega) \\ \vdots \\ J_S^\tau(\mathbf{r}_t, \omega) \end{bmatrix} \quad (2)$$

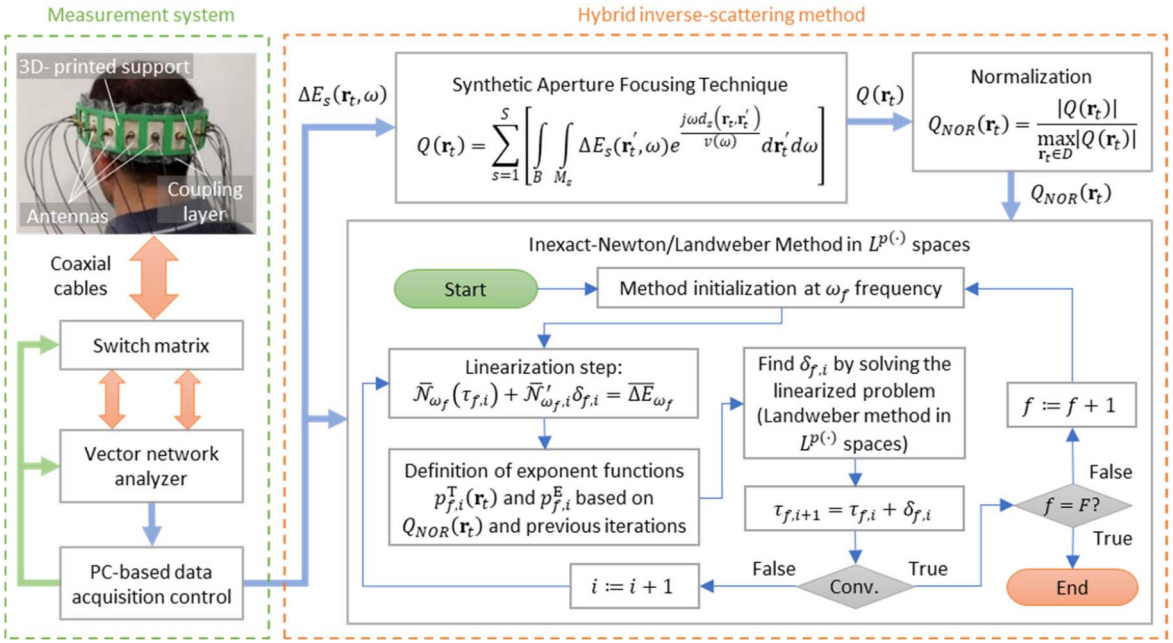

FIGURE 2. Block diagram of the whole inverse scattering approach for brain injury detection and monitoring. Building blocks of the measurement system prototype (left) and hybrid data processing technique (right).

where $J_s^\tau(\mathbf{r}_t,\omega)=j\omega\epsilon_b(\omega)\tau(\mathbf{r}_t,\omega)E_{s1}(\mathbf{r}_t,\omega)$. The actual permittivity $\epsilon_{t1}(\mathbf{r}_t,\omega)$ being unknown, $J_s^\tau(\mathbf{r}_t,\omega)$, $\tau(\mathbf{r}_t,\omega)$ and $E_{s1}(\mathbf{r}_t,\omega)$ turn out to be unknown quantities as well for $\mathbf{r}_t\in D$. In particular, $E_{s1}(\mathbf{r}_t,\omega)$, which represents the total electric field of the actual configuration, depends on the value of $\tau(\mathbf{r}_t,\omega)$.

If we suppose that, between the reference and the actual configuration, everything is unchanged except the target inside the investigation domain D, i.e., $\epsilon(\mathbf{r}_t,\omega)=\epsilon_{t0}(\mathbf{r}_t,\omega)$, $\mathbf{r}_t\notin D$, the difference field between these two situations is given by

$$\Delta E_s(\mathbf{r}_t,\omega)=j\omega\mu_0\int_D J_s^\tau\left(\mathbf{r}_t',\omega\right)G\left(\mathbf{r}_t,\mathbf{r}_t',\omega\right)d\mathbf{r}_t' \tag{3}$$

where $G\left(\mathbf{r}_t,\mathbf{r}_t',\omega\right)$, i.e., the Green's function, is the solution of the following inhomogeneous differential equation:

$$\left[\nabla^2+\omega^2\mu_0\epsilon_{t0}(\mathbf{r}_t,\omega)\right]G\left(\mathbf{r}_t,\mathbf{r}_t',\omega\right)=\delta\left(\mathbf{r}_t-\mathbf{r}_t'\right) \tag{4}$$

in which $\delta(\mathbf{r}_t-\mathbf{r}_t')$ is a Dirac's delta function centered at $\mathbf{r}_t'$. Please note that, since inside $J_s^\tau(\mathbf{r}_t,\omega)$ the contrast function multiplies the electric field of the actual configuration, (3) establishes a nonlinear relationship between the difference field $\Delta E_s(\mathbf{r}_t,\omega)$ and the values of $\tau(\mathbf{r}_t,\omega)$. With a shorter notation, this fact can be expressed as $\Delta E_s(\mathbf{r}_t,\omega)=\mathcal{N}_s(\tau)(\mathbf{r}_t,\omega)$, where $\mathcal{N}_s$ is a nonlinear operator that maps the contrast function on difference electric field measurements for the sth view. When all views are considered, a system of nonlinear equations is formed as

$$\begin{bmatrix}\mathcal{N}_1(\tau)(\mathbf{r}_t,\omega)\\ \vdots\\ \mathcal{N}_S(\tau)(\mathbf{r}_t,\omega)\end{bmatrix}=\begin{bmatrix}\Delta E_1(\mathbf{r}_t,\omega)\\ \vdots\\ \Delta E_S(\mathbf{r}_t,\omega)\end{bmatrix} \tag{5}$$

Here, the right-hand side is a column vector containing the available data (in each row, $\mathbf{r}_t\in M_s$, $s=1,\ldots,S$), whereas $\tau(\mathbf{r}_t,\omega)$, with $\mathbf{r}_t\in D$, is the main unknown. The result is a nonlinear inverse scattering problem, written in compact way as $\overline{\mathcal{N}}_\omega(\tau)=\overline{\Delta E}_\omega$, where $\overline{\Delta E}_\omega\in\mathrm{E}$ (data space), $\tau\in\mathrm{T}$ (space of unknown), and a nonlinear operator is defined such that $\overline{\mathcal{N}}_\omega:\mathrm{T}\to\mathrm{E}$. The solution strategy is outlined in the following Sections.

B. OUTLINE OF THE HYBRID INVERSION PROCEDURE

The task of retrieving the contrast function $\tau(\mathbf{r}_t,\omega)$ from (5) is accomplished by means of a hybrid inversion procedure, whose goal is to combine a fast qualitative processing with an accurate quantitative reconstruction approach. A block diagram of the proposed method, which also comprises the main parts of the data acquisition system, is visible in Fig. 2.

During monitoring phase, the total field measurements acquired with the reference configuration are subtracted in order to compute $\Delta E_s(\mathbf{r}_t,\omega)$, $s=1,\ldots,S$. The difference field data retrieved in this way are firstly processed by a Synthetic Aperture Focusing Technique (SAFT) [29]–[31], where a qualitative image of the internal changes in the head cross section is obtained. This processing step, detailed in Section II-C, is very fast and produces an output image $Q(\mathbf{r}_t)$, $\mathbf{r}_t\in D$, which is subsequently normalized with respect to its maximum value. The resulting normalized indicator function $Q_{NOR}(\mathbf{r}_t)$ assumes values proximal to unity where significant changes in complex permittivity are detected between ϵ_{t0} and ϵ_{t1} (in other words, where contrast function τ significantly differs from zero), and lower values otherwise.

The next step of the hybrid procedure is quantitative inversion. To this end, a variable-exponent Lebesgue-space setting

is considered, where the information conveyed by the normalized qualitative indicator function $Q_{NOR}(\mathbf{r}_t)$ is exploited to build an initial map of the exponent function of the space of unknown. The processing method belongs to the inexact-Newton class, and a Landweber-type algorithm in $L^{p(\cdot)}$ spaces is used as an inner loop. In addition, the quantitative technique incorporates a frequency-hopping strategy. The final result is a pointwise characterization of the contrast function $\tau(\mathbf{r}_t, \omega)$, which quantitatively describes the variations in the dielectric properties of patient's head between reference and actual configuration. A detailed description of the whole reconstruction process is presented in Section II-D.

C. CONSTRUCTION OF AN APPROXIMATE QUALITATIVE MAP

In the first step, a SAFT technique is applied to the set of measured difference field data, $\Delta E_s(\mathbf{r}_t, \omega)$, $\mathbf{r}_t \in M_s$, $s = 1, \ldots, S$, to retrieve a qualitative indicator function $Q(\mathbf{r}_t)$, $\mathbf{r}_t \in D$, which allows an initial estimation of location and size of the detected inhomogeneity inside head. In particular, the indicator function is given by

$$Q(\mathbf{r}_t) = \sum_{s=1}^{S} \left[\int_B \int_{M_s} \Delta E_s(\mathbf{r}'_t, \omega) e^{\frac{j\omega d_s(\mathbf{r}_t, \mathbf{r}'_t)}{v(\omega)}} d\mathbf{r}'_t d\omega \right], \quad (6)$$

where $\mathbf{r}_t \in D$, $B = [\omega_{min}, \omega_{max}]$ is the angular frequency band where electric field is collected, $d_s(\mathbf{r}_t, \mathbf{r}'_t) = \|\mathbf{r}_t - \mathbf{r}'_t\| + \|\mathbf{r}_t - \mathbf{r}^s_t\|$, and $v(\omega) = (\mu_0 \Re\{\epsilon_g(\omega)\})^{-1/2}$ is the frequency-dependent wave propagation velocity, $\epsilon_g(\omega)$ being an estimation of the average complex permittivity of the background medium. In the cases presented in this article, $\epsilon_g(\omega)$ is taken as the Debye model of the external coupling medium, which has similar properties to the internal head tissues.

It is worth noting that the SAFT formula in (6) is similar to the orthogonality sampling method (OSM), introduced in [32] and recently physically interpreted in [33], [34]. Basically, in the OSM, the phase shifting term in the SAFT indicator function (6) is replaced by another phase factor, which is related to the far field pattern of the Green's function. Indeed, both methods provide an indicator function that assumes high values in the points belonging to the targets, which represent dielectric discontinuities in the propagation medium. Therefore, the OSM will be also considered in future works as a possible efficient alternative for obtaining a more accurate initial qualitative estimation $Q(\mathbf{r}_t)$ of the inhomogeneities inside patient's head.

A normalized indicator function $Q_{NOR}(\mathbf{r}_t)$ is then calculated as $Q_{NOR}(\mathbf{r}_t) = |Q(\mathbf{r}_t)|/\max_{\mathbf{r}_t \in D} |Q(\mathbf{r}_t)|$ for $\mathbf{r}_t \in D$. This function then assumes values between 0 (where no inhomogeneities are detected with respect to the background) and 1 (around the approximate location of the brain injury).

D. QUANTITATIVE INVERSION IN VARIABLE-EXPONENT SETTING

The quantitative step is built around an inexact-Newton algorithm, whose scheme is drafted in Fig. 2. As to the input data, we assume that field measurements at F different angular frequencies $\omega_{min} = \omega_1 < \omega_2 < \cdots < \omega_F = \omega_{max}$ in the considered band B are available ($\overline{\Delta E}_{\omega_f}, f = 1, \ldots, F$). These data are exploited inside a frequency-hopping approach, where the inverse problem is solved starting from $f = 1$, using the results as a-priori information for the following reconstruction steps, time after time.

At $\omega = \omega_f$, the method is initialized with a contrast function equal to $\tau_{1,1} = 0$ for $f = 1$, whereas in the subsequent frequencies ($f > 1$) the initial guess is obtained by scaling the previous reconstruction result $\overline{\tau}_{f-1}$ with respect to frequency, i.e., $\tau_{f,1} = \{\Re[\overline{\tau}_{f-1}\epsilon_b(\omega_{f-1})] + j\Im[\overline{\tau}_{f-1}\epsilon_b(\omega_{f-1})]\}/\epsilon_b(\omega_f)$.

After that, the inexact-Newton loop starts, whose iterations are indicated with index $i = 1, 2, \ldots, I$. In each step, the equation $\overline{\mathcal{N}}_{\omega_f}(\tau) = \overline{\Delta E}_{\omega_f}$ defined in Section II-A is linearized around $\tau_{f,i}$ by means of the Fréchet derivative of the nonlinear operator $\overline{\mathcal{N}}_{\omega_f}$ (denoted here as $\overline{\mathcal{N}}'_{\omega_f,i}$). As a result, the linear equation

$$\overline{\mathcal{N}}_{\omega_f}(\tau_{f,i}) + \overline{\mathcal{N}}'_{\omega_f,i}\delta_{f,i} = \overline{\Delta E}_{\omega_f} \quad (7)$$

is obtained, where $\delta_{f,i} \in \mathrm{T}$ is the unknown of the linearized problem, which is found by a truncated Landweber-type method in $L^{p(\cdot)}$ spaces [35].

The inner loop solves (7) in a regularized way by considering the space of unknown as a variable-exponent Lebesgue space $\mathrm{T} \in L^{p(\cdot)}$, with $p(\cdot) = p^{\mathrm{T}}_{f,i}(\mathbf{r}_t)$, $\mathbf{r}_t \in D$, where the corresponding exponent function depends on the position inside the investigation domain D. The data space $\mathrm{E} \in L^p$ is a fixed-exponent Lebesgue space with $p = p^{\mathrm{E}}_{f,i}$. Indeed, a key point of the hybrid approach is the definition of these exponent functions $p^{\mathrm{T}}_{f,i}(\mathbf{r}_t)$ and $p^{\mathrm{E}}_{f,i}$. The exponent function of the space T, which is a function of $\mathbf{r}_t$ inside D, is calculated for each Newton linearization step and for each frequency value taking into account the qualitative reconstruction $Q_{NOR}(\mathbf{r}_t)$ and the results of previous iterations as follows:

$$p^{\mathrm{T}}_{f,i}(\mathbf{r}_t) = \begin{cases} p_s + \Delta p Q_{NOR}(\mathbf{r}_t), & i = 1, f = 1 \\ p_s + \Delta p \frac{|\overline{\tau}_{f-1}(\mathbf{r}_t)|}{\max_{\mathbf{r}\in D}|\overline{\tau}_{f-1}(\mathbf{r}_t)|}, & i = 1, f > 1 \\ p_s + \Delta p \frac{|\tau_{f,i-1}(\mathbf{r}_t)|}{\max_{\mathbf{r}\in D}|\tau_{f,i-1}(\mathbf{r}_t)|}, & i > 1 \end{cases} \quad (8)$$

where p_s is the minimum value of the function, and Δp the extent of its variation inside D. In other words, $p^{\mathrm{T}}_{f,i}(\mathbf{r}_t)$ is chosen such that:

- At the beginning of nonlinear inversion, $p^{\mathrm{T}}_{f,i}$ is maximum where the qualitative step of Section II-C found relevant inhomogeneities with respect to the background, i.e., where the injury is located;
- When the algorithm starts with a new frequency, $p^{\mathrm{T}}_{f,i}$ is linearly connected to the normalized contrast function magnitude at the previous frequency step;
- Inside each Newton loop, $p^{\mathrm{T}}_{f,i}$ is chosen based on the contrast function magnitude retrieved at the previous linearization step.

As to the exponent function in the data space E, it is chosen as the spatial average value of $p^{\mathrm{T}}_{f,i}(\mathbf{r}_t)$ for $\mathbf{r}_t \in D$,

that is

$$p_{f,i}^{\mathrm{E}} = \frac{1}{\mu(D)} \int_D p_{f,i}^{\mathrm{T}}(\mathbf{r}_t) d\mathbf{r}_t \tag{9}$$

where $\mu(D)$ indicates the measure of the investigation domain D. Both maps are therefore adaptively defined for each Newton step and are kept fixed for the inner Landweber loop. The inner iterations (indicated with index $l = 1, 2, \ldots, L$) start with initial guess $\delta_{f,i,1} = 0$ and are structured as

$$\delta_{f,i,l+1} = J_{\mathrm{T}^*}^{p_{f,i}^{\mathrm{T}*}} \Big\{ J_{\mathrm{T}}^{p_{f,i}^{\mathrm{T}}}(\delta_{f,i,l}) + \beta \overline{\mathcal{N}}'^{*}_{\omega_f,i} J_{\mathrm{E}}^{p_{f,i}^{\mathrm{E}}} \Big(\overline{\Delta E}_{\omega_f} - \overline{\mathcal{N}}_{\omega_f}(\tau_{f,i}) - \overline{\mathcal{N}}'_{\omega_f,i} \delta_{f,i,l} \Big) \Big\} \tag{10}$$

where $\overline{\mathcal{N}}'^{*}_{\omega_f,i}$ is the adjoint of the linear operator $\overline{\mathcal{N}}'_{\omega_f,i}$, $J_{\Omega}^{p(\cdot)}$ represents the duality map of Lebesgue space Ω with exponent $p(\cdot)$, $\beta = 1/\|\overline{\mathcal{N}}'_{\omega_f,i}\|^2$ is the step size, and $p_{f,i}^{\mathrm{T}*}$ is the point-wise Hölder conjugate of $p_{f,i}^{\mathrm{T}}$ [36].

When a suitable solution $\delta_{f,i} = \delta_{f,i,L}$ is found inside the inner loop, the estimate of the unknown function is updated as

$$\tau_{f,i+1} = \tau_{f,i} + \delta_{f,i} \tag{11}$$

The outermost frequency-hopping loop is terminated when data at the last frequency have been used ($f = F$). The numbers of performed inexact-Newton and Landweber iterations (I and L, respectively) are defined as the minimum values between those satisfying a stopping threshold based on the relative variation of the data residual (denoted by Δr) and the predefined maximum numbers of iterations (I_M and L_M, respectively).

III. NUMERICAL RESULTS

The proposed diagnostic method has been firstly tested by processing synthetic data obtained in 3D configurations. Brain injuries mimicking hemorrhagic strokes have been emulated inside the head of the *AustinWoman* voxel-based model [37]. The dielectric properties of tissues inside the numerical phantom have been characterized by means of third- and fourth-order Debye models, when available [38], [39]. The internal stroke geometries have been inspired by the analysis of an open-source collection of segmented MRI images of stroke-affected patients [40]. In order to define the stroke lesion inside head, white matter tissues have been replaced with the dielectric properties of blood in a region given by the subtraction between two ellipsoids. This allows the creation of realistic shapes with irregular borders. The first ellipsoid has its center in $\mathbf{r}_i = (x_i, y_i, z_i)$ and has semiaxes of length a_i, b_i and c_i. The second one (whose volume is subtracted from the first) has the same size and is centered at $\mathbf{r}_h = (x_i + (d-2)a_i, y_i, z_i)$, where d indicates a percentage shift on the x axis. The head phantom is immersed in a matching medium characterized by a complex dielectric permittivity ϵ_b, whose dielectric properties follow the Debye model of 70:30 glycerin:water mixture presented in [28] and are reported in Fig. 3. A set of $S = 16$ positions around the numerical head phantom has been considered to define the measurement domain. These locations lie on an horizontal ellipse at $z = 0.187$ m, whose x and y axes have dimensions $d_x = 0.184$ m and $d_y = 0.22$ m, respectively. In numerical results, the reference distribution of the dielectric permittivity $\epsilon_{t0}(\mathbf{r}_t, \omega)$ is taken as the healthy head.

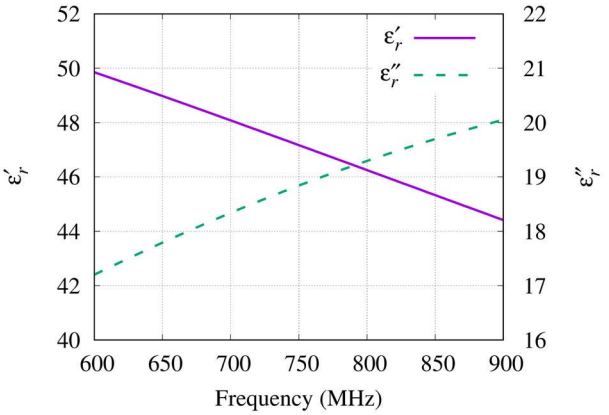

FIGURE 3. Complex relative dielectric permittivity of the 70:30 glycerin:water mixture adopted as coupling medium in both numerical simulations and experiments, according to the Debye model in [28].

The field values have been computed in time domain by means of the finite-difference time-domain (FDTD) software *gprMax* [41], which is an open-source package for electromagnetic simulation [42]. The 3D forward simulation domain has been partitioned into 3.408×10^6 cubic cells of 2-mm side, and its extension is 0.284 m (142 cells) × 0.320 m (160 cells) × 0.284 m (142 cells) on x, y, and z directions, respectively. All around the FDTD simulation domain, absorbing boundary conditions have been implemented with a 10-cells wide perfectly matched layer. The evolution of electromagnetic fields in time domain has been simulated for a time interval of $T = 3 \times 10^{-8}$ s, with a time step of 3.85×10^{-12} s. In a multiview arrangement, each of the S previously defined locations around the head is in turn occupied by a Hertzian dipole source (z-polarized), whereas the other ones are used to sample the z component of the electric field (measurement domain M_s, $s = 1, \ldots, S$). The transmitting antennas are fed by Gaussian derivative waveform with central frequency of 1 GHz. After FDTD simulations, data in frequency domain have been extracted by a Fast Fourier Transform (FFT). In particular, $F = 7$ frequency values, uniformly distributed in the band [600, 900] MHz have been considered. The computed values of $\overline{\Delta E}_{\omega_f}$, $f = 1, \ldots, F$, have been corrupted with an additive Gaussian noise with zero mean value and $SNR = 25$ dB. The numerical simulations have been performed on a workstation equipped with an Intel Core i7-2600K CPU at 3.40 GHz, 8 GB of RAM, and a NVIDIA GeForce GTX 650 GPU with 1 GB RAM, which has also been used to run the inversion method. Forward simulations required a computational time of 449 s

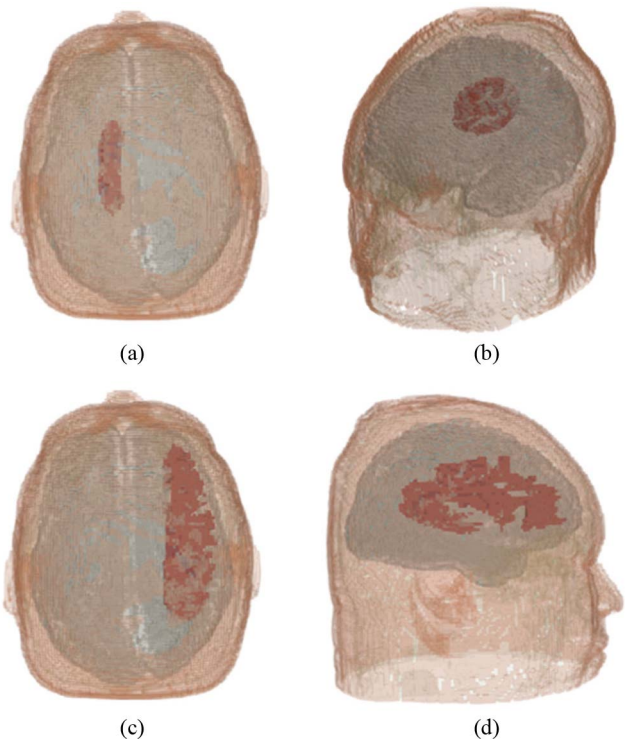

FIGURE 4. Three-dimensional numerical phantoms of stroke-affected head. First test case: (a) Top view, (b) side view. Second test case: (c) Top view, (d) side view.

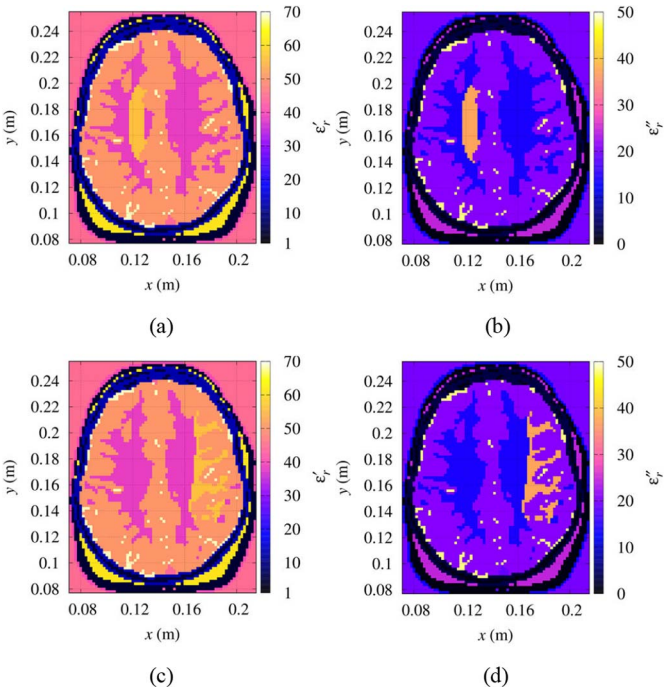

FIGURE 5. Complex relative dielectric permittivity at 900 MHz on a cross-sectional slice at $z = 0.187$ m of the stroke-affected head phantoms. First test case: (a) Real part, (b) imaginary part. Second test case: (c) Real part, (d) imaginary part.

approximately for each view, with a peak usage of 592 MB of main RAM and 741 MB of GPU RAM.

A. FIRST TEST CASE

The first case of brain injury comprises a stroke of medium size (semiaxes $a_i = 0.01$ m, $b_i = 0.03$ m, $c_i = 0.02$ m) located at $\mathbf{r}_i = (0.125,\ 0.169, 0.187)$ m, with $d = 0.7$. The 3D model of the head is visible in Fig. 4(a) and Fig. 4(b), which show that the hemorrhagic inclusion is quite deep inside phantom's brain. A cross-sectional view of the complex relative dielectric permittivity on the xy plane located at the stroke center ($z = 0.187$ m) is also reported in Fig. 5(a)-(b).

With reference to Section II-D, the inversion algorithm has been run with exponent parameters $p_s = 1.4$, $\Delta p = 0.6$, maximum number of iterations $I_M = 50$, $L_M = 100$, and residual variation threshold $\Delta r = 0.01$. The whole inversion method required a computational time of 174 s (45 s for each processed frequency, approximately) and a peak usage of 40 MB of RAM. Reconstruction results are shown in Fig. 6(a)-(c). In details, Fig. 6(a) reports the qualitative indicator Q_{NOR}, whereas the subsequent figures are related to the quantitative inversion, reporting the reconstructed contrast at 900 MHz. Clearly, the stroke location is correctly detected by the qualitative step (despite the presence of background artefacts) and the final result is a quite accurate description of the contrast function inside the investigation domain D (the actual value of $\tau\epsilon_{r,b}$ inside the stroke at 900 MHz is equal to $17.49 - j22.82$).

The overall quality of the dielectric reconstruction has been assessed through the following performance metrics, which measure the difference between the reconstructed contrast function and its actual value:

$$e\begin{Bmatrix} bkg \\ tar \end{Bmatrix} = \frac{1}{\mu\left(D\begin{Bmatrix} bkg \\ tar \end{Bmatrix}\right)} \int_{D\begin{Bmatrix} bkg \\ tar \end{Bmatrix}} \frac{|\tau(\mathbf{r}_t) - \tau_{actual}(\mathbf{r}_t)|}{|\tau_{actual}(\mathbf{r}_t) + 1|} d\mathbf{r}_t \tag{12}$$

where e_{bkg} and e_{tar} are the relative reconstruction errors on the background and inside the brain lesion, respectively (represented by regions D_{bkg} and D_{tar}, μ being the corresponding measure).

The behavior of these quantities in the various frequency-hopping steps of the inversion procedure is reported in Fig. 7, in comparison with the results provided by the standard variable-exponent approach [28]. Several interesting facts can be noticed. First, both error metrics are lower with the proposed hybrid method, although a greater difference is observable in background error e_{bkg}. Moreover, the error computed inside the brain lesion e_{tar} decreases as the considered frequencies become higher, whereas the background error e_{bkg} exhibits small changes among the various frequency steps.

B. SECOND TEST CASE

In the second set of numerical simulations, a larger stroke-mimicking inclusion has been considered, where the main ellipsoid has semiaxes $a_i = 0.021$ m, $b_i = 0.06$ m,

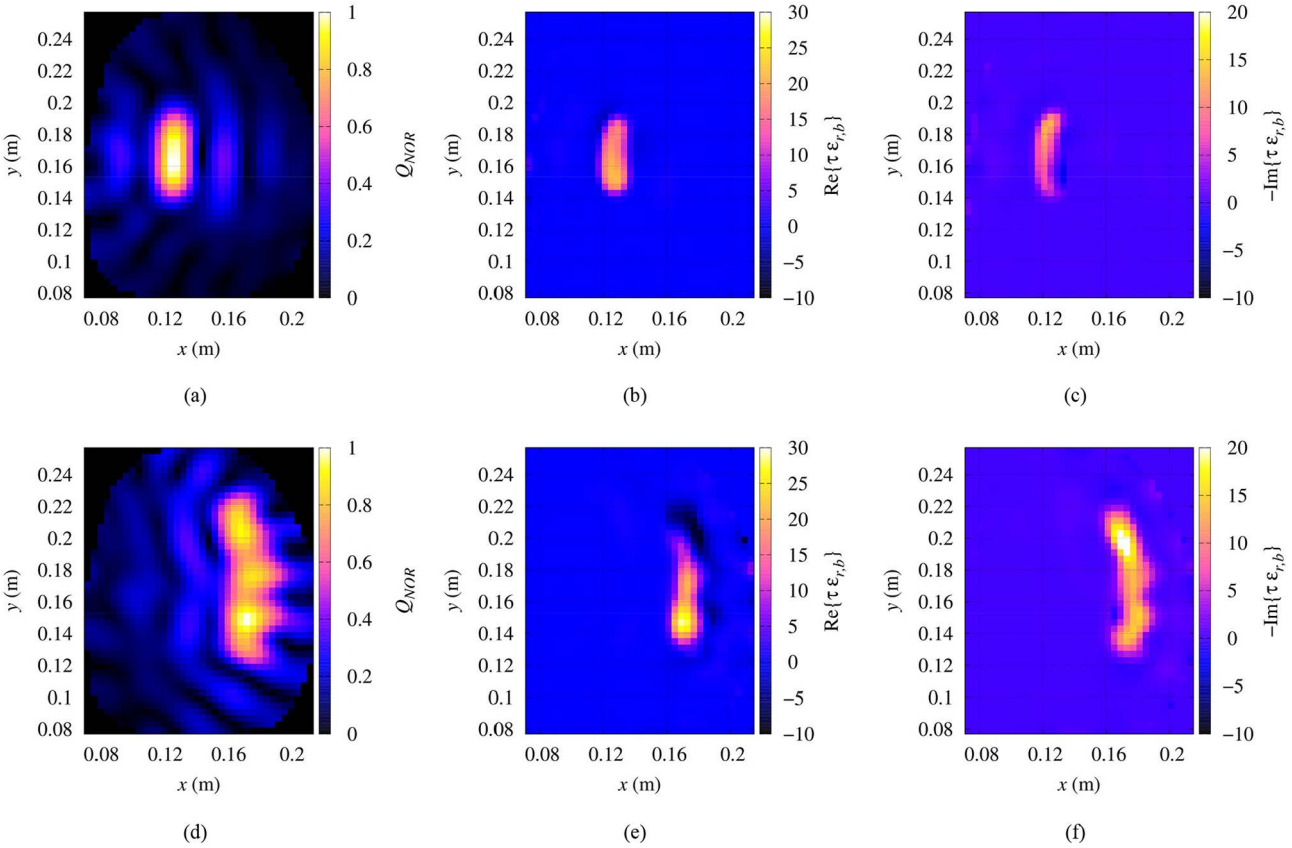

FIGURE 6. Numerical results. First test case: (a) qualitative map; (b) real and (c) imaginary part of $\tau\epsilon_{r,b}$ in the last frequency-hopping step (900 MHz). Second test case: (d) qualitative map; (e) real and (f) imaginary part of $\tau\epsilon_{r,b}$ at 900 MHz.

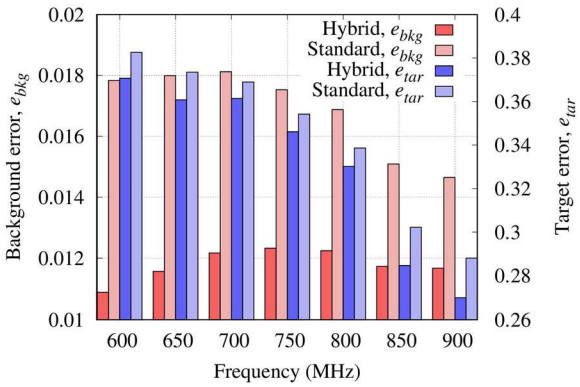

FIGURE 7. Numerical results, first test case. Relative reconstruction errors on the background (e_{bkg}) and on the target (e_{tar}) versus frequency. Comparison between the proposed approach and the standard method [28].

$c_i = 0.03$ m, $d = 0.7$, and it is centered at the point $\mathbf{r}_i = (0.175,\ 0.189, 0.177)$ m. The resulting 3D shape of the stroke is highly irregular and significantly different from the previous case, as shown in Fig. 4(c)-(d). It is worth noting that this kind of hemorrhage appears quite large as seen in transparence from the top, but it presents several internal voids, as visible in Fig. 4(d). This very complicate structure, which of course makes the detection more challenging, is also evident from the distribution of the complex relative dielectric permittivity on a horizontal slice at $z = 0.187$ m reported in Fig. 5(c)-(d). The contrast function inside the stroke is the same as in Section III-A.

With the same inversion method parameters as the previous case, results are shown in Fig. 6(d)-(f). As before, the qualitative map Q_{NOR} provides a good approximation of both the stroke position and its extent. The quantitative inversion is more challenging than before, due to the lesion shape. An artifact appears on the top of the real part of τ, due to the highly irregular conformation of the target. However, a good overall estimation of the dielectric properties is found.

In Fig. 8, the relative reconstruction errors are plotted and again compared with [28]. Even here, both error metrics are always lower with the proposed approach. Differently from the first test case, however, errors are averagely higher and e_{bkg} slightly increases with frequency. This can be ascribed to the increased size of the stroke, which leads to more background artefacts. The observed trends of the target error e_{tar} show no significant differences with respect to the first test case.

IV. INITIAL EXPERIMENTAL VALIDATION

The microwave imaging method proposed in this article has also been validated against experimental data. The measurement setup, shown in Fig. 9(a), includes a vector network

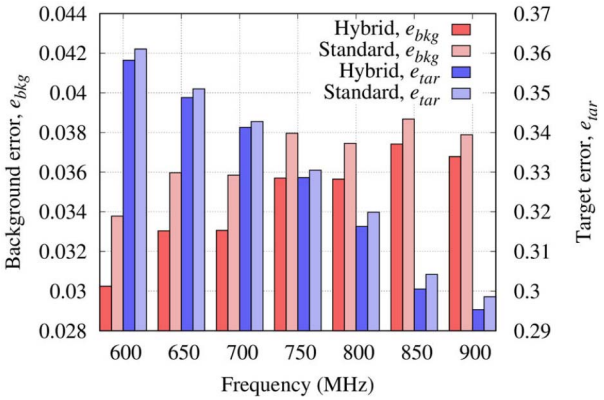

FIGURE 8. Numerical results, second test case. Relative reconstruction errors on the background (e_{bkg}) and on the target (e_{tar}) versus frequency. Comparison between the proposed approach and the standard method [28].

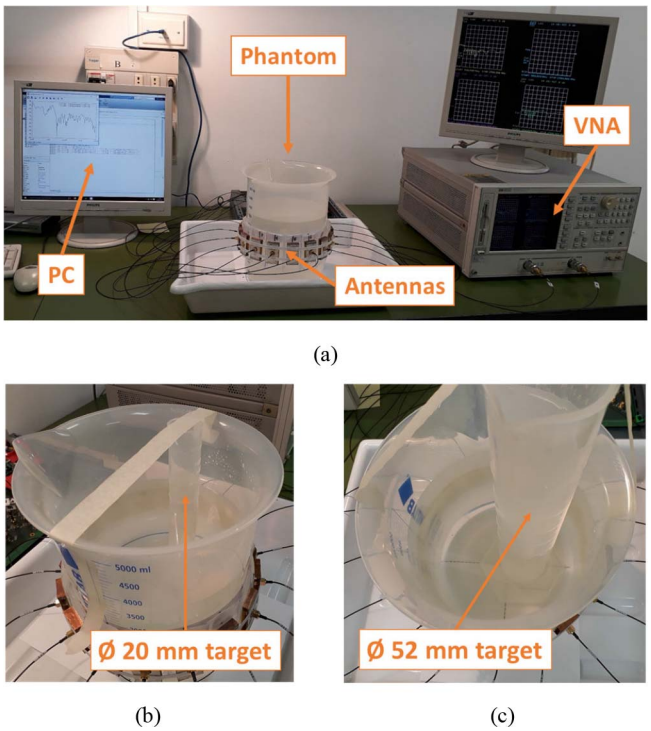

FIGURE 9. Configuration adopted for the initial experimental validation: (a) picture of the measurement setup; (b) First phantom; (c) Second phantom.

analyzer (VNA), a switch matrix (not visible in the photograph), a control personal computer (PC), and $S = 16$ cavity-backed bowtie-like antennas [27] placed in contact with the phantom through bags filled by a 70:30 glycerin:water mixture [43].

In these initial tests, the phantom is a liquid-filled laboratory beaker with cylindrical inclusions, which defines a very simple and reproducible model of a cross section of the head affected by hemorrhagic stroke. The characteristics of the adopted containers are listed in Table 1. In particular, two different phantom configurations were tested. The first phantom [Fig. 9(b)] is built placing Cylinder #2 (20-mm graduated cylinder, filled with a 0.9% saline solution) inside Cylinder #1 (laboratory beaker, filled with 70:30 glycerin:water mixture) at the position reported in Table 1. The second phantom [Fig. 9(c)] presents Cylinder #3 (52-mm graduated cylinder, filled with a 0.9% saline solution) inside Cylinder #1 as external container.

TABLE 1. Characteristics of the simplified targets adopted in the initial experimental validation of the hybrid method.

	Cylinder #1	Cylinder #2	Cylinder #3
Capacity	5 L	100 mL	500 mL
Type	Laboratory beaker	Graduated cylinder	Graduated cylinder
Center position	(0, 0) mm	(45, 0) mm	(25, 0) mm
Diameter	180 mm	20 mm	52 mm
Material	Polypropylene	Polypropylene	Polypropylene
Filling liquid	70:30 glycerin: water mixture	0.9% saline solution	0.9% saline solution

The reference configuration is a homogeneous cylinder with 180 mm diameter and dielectric permittivity $\epsilon_{t0}(\mathbf{r}_t, \epsilon)$ given by the Debye model of 70:30 glycerin:water mixture from [28]. The result of the method validation with these experimental configurations is reported in Fig. 10 (white circles indicate the true profiles). In particular, the first and the second row concern the two different phantoms. Parameters are the same as Section III, except for $\Delta r = 0.3$.

As to the first case (small inclusion, Cylinder #2) an already good qualitative image is obtained [Fig. 10(a)], which is followed by a correct reconstruction of the dielectric properties inside the quantitative step. Artefacts of small intensity can be noticed on the background, but the inclusion size and its properties are characterized quite well (the actual value of $\tau\epsilon_{r,b}$ at 900 MHz is equal to $29.15 - j16.66$ approximately). The second phantom (medium-size inclusion, Cylinder #3) evidences a more involved reconstruction, since the qualitative map presents more artefacts and an imperfect estimation of the target. An underestimation of the target size can be observed also inside the reconstructed dielectric properties at 900 MHz. Nevertheless, is also evident that, despite the rather low quality of the initial qualitative map, the inversion method has been able to identify the target.

V. CONCLUSION

Brain injuries constitute a life-threatening event where patients' health benefits from a rapid on-site diagnosis. In the context of emerging electromagnetic technologies, a microwave approach to the imaging of brain injuries has been pursued in this article. A new hybrid tomographic strategy that combines qualitative and quantitative inversion has been introduced. In particular, the information provided by a synthetic-aperture method has been integrated with a nonlinear variable-exponent algorithm in Lebesgue spaces, in order to define the exponent function in a more effective way. The proposed inverse-scattering method has been validated

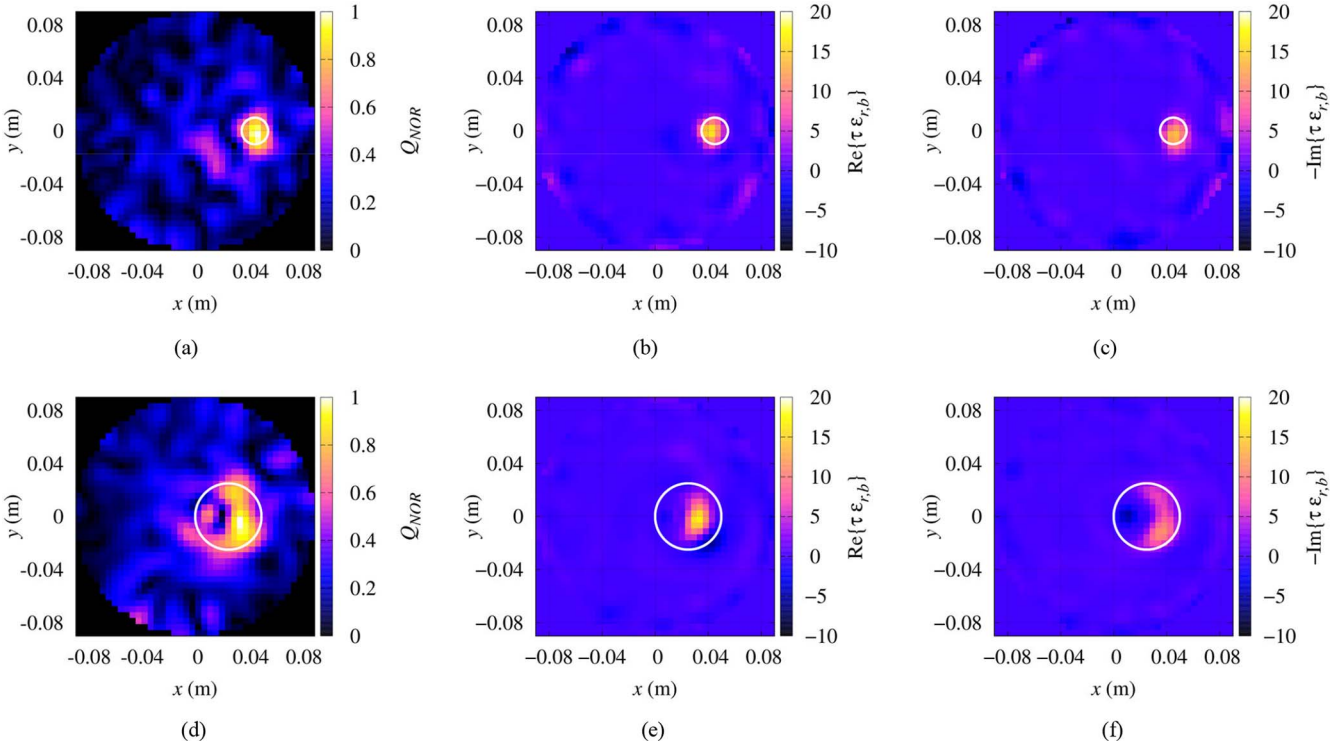

FIGURE 10. Experimental results. First phantom: (a) qualitative map; (b) real and (c) imaginary part of $\tau\epsilon_{r,b}$ in the last frequency-hopping step (900 MHz). Second phantom: (d) qualitative map; (e) real and (f) imaginary part of $\tau\epsilon_{r,b}$ at 900 MHz.

with three-dimensional numerical simulations involving realistic head models, as well as against experimental data, measured with an initial prototype applied on simplified targets. Results are promising, although the reconstruction of large and irregularly shaped lesions may be improved. Trials with more realistic experimental phantoms, and the extension to a fully three-dimensional setting will be also considered as future developments.

ACKNOWLEDGMENT

The authors would like to acknowledge the contribution of L. Oddone and S. Sacco (University of Genoa, Italy) in defining the stroke-affected head models used inside numerical simulations.

REFERENCES

[1] M. Katan and A. Luft, "Global burden of stroke," *Seminars Neurol.*, vol. 38, no. 2, pp. 208–211, Apr. 2018.

[2] C. O. Johnson *et al.*, "Global, regional, and national burden of stroke, 1990–2016: A systematic analysis for the global burden of disease study 2016," *Lancet Neurol.*, vol. 18, no. 5, pp. 439–458, May 2019.

[3] H. A. Lumley *et al.*, "A scoping review of pre-hospital technology to assist ambulance personnel with patient diagnosis or stratification during the emergency assessment of suspected stroke," *BMC Emerg. Med.*, vol. 20, no. 1, p. 30, Apr. 2020.

[4] A. Fhager, S. Candefjord, M. Elam, and M. Persson, "Microwave diagnostics ahead: Saving time and the lives of trauma and stroke patients," *IEEE Microw. Mag.*, vol. 19, no. 3, pp. 78–90, May 2018.

[5] M. Pastorino and A. Randazzo, *Microwave Imaging Methods and Applications*. Boston, MA, USA: Artech House, 2018.

[6] L. Crocco, I. Karanasiou, M. James, and R. C. Conceição, *Emerging Electromagnetic Technologies for Brain Diseases Diagnostics, Monitoring and Therapy*. Cham, Switzerland: Springer, 2018.

[7] A. S. M. Alqadami, K. S. Bialkowski, A. T. Mobashsher, and A. M. Abbosh, "Wearable electromagnetic head imaging system using flexible wideband antenna array based on polymer technology for brain stroke diagnosis," *IEEE Trans. Biomed. Circuits Syst.*, vol. 13, no. 1, pp. 124–134, Feb. 2019.

[8] M. S. R. Bashri and T. Arslan, "Low-cost and compact RF switching system for wearable microwave head imaging with performance verification on artificial head phantom," *IET Microw. Antennas Propag.*, vol. 12, no. 5, pp. 706–711, Apr. 2018.

[9] R. Joshi *et al.*, "Analysis and design of dual-band folded-shorted patch antennas for robust wearable applications," *IEEE Open J. Antennas Propag.*, vol. 1, pp. 239–252, 2020.

[10] J. Blauert and A. Kiourti, "Bio-matched antennas with flare extensions for reduced low frequency cutoff," *IEEE Open J. Antennas Propag.*, vol. 1, pp. 136–141, 2020.

[11] M. Persson *et al.*, "Microwave-based stroke diagnosis making global prehospital thrombolytic treatment possible," *IEEE Trans. Biomed. Eng.*, vol. 61, no. 11, pp. 2806–2817, Nov. 2014.

[12] G. Zhu, A. Bialkowski, L. Guo, B. Mohammed, and A. Abbosh, "Stroke classification in simulated electromagnetic imaging using graph approaches," *IEEE J. Electromagn., RF, Microwav. Med. Biol.*, early access, May 18, 2020, doi: 10.1109/JERM.2020.2995329.

[13] S. Mustafa, B. Mohammed, and A. Abbosh, "Novel preprocessing techniques for accurate microwave imaging of human brain," *IEEE Antennas Wireless Propag. Lett.*, vol. 12, pp. 460–463, 2013.

[14] A. T. Mobashsher, A. Mahmoud, and A. M. Abbosh, "Portable wideband microwave imaging system for intracranial hemorrhage detection using improved back-projection algorithm with model of effective head permittivity," *Sci. Rep.*, vol. 6, Feb. 2016, Art. no. 20459.

[15] R. Scapaticci, J. Tobon, G. Bellizzi, F. Vipiana, and L. Crocco, "Design and numerical characterization of a low-complexity microwave device for brain stroke monitoring," *IEEE Trans. Antennas Propag.*, vol. 66, no. 12, pp. 7328–7338, Dec. 2018.

[16] J. A. Tobon Vasquez *et al.*, "A prototype microwave system for 3D brain stroke imaging," *Sensors*, vol. 20, no. 9, p. 2607, Jan. 2020.

[17] S. Y. Semenov and D. R. Corfield, "Microwave tomography for brain imaging: Feasibility assessment for stroke detection," *Int. J. Antennas Propag.*, vol. 2008, May 2008, Art. no. 254830.
[18] M. Hopfer, R. Planas, A. Hamidipour, T. Henriksson, and S. Semenov, "Electromagnetic tomography for detection, differentiation, and monitoring of brain stroke: A virtual data and human head phantom study," *IEEE Antennas Propag. Mag.*, vol. 59, no. 5, pp. 86–97, Oct. 2017.
[19] L. Guo and A. Abbosh, "Stroke localization and classification using microwave tomography with k-means clustering and support vector machine," *Bioelectromagnetics*, vol. 39, no. 4, pp. 312–324, 2018.
[20] V. L. Coli *et al.*, "Detection of simulated brain strokes using microwave tomography," *IEEE J. Electromagn., RF, Microwav. Med. Biol.*, vol. 3, no. 4, pp. 254–260, Dec. 2019.
[21] O. Karadima *et al.*, "Experimental validation of microwave tomography with the DBIM-TwIST algorithm for brain stroke detection and classification," *Sensors*, vol. 20, no. 3, p. 840, Jan. 2020.
[22] L. Li, L. G. Wang, F. L. Teixeira, C. Liu, A. Nehorai, and T. J. Cui, "DeepNIS: Deep neural network for nonlinear electromagnetic inverse scattering," *IEEE Trans. Antennas Propag.*, vol. 67, no. 3, pp. 1819–1825, Mar. 2019.
[23] L. Li, L. G. Wang, and F. L. Teixeira, "Performance analysis and dynamic evolution of deep convolutional neural network for electromagnetic inverse scattering," *IEEE Antennas Wireless Propag. Lett.*, vol. 18, pp. 2259–2263, 2019.
[24] M. Wang, H. Li, Y. Shuang, and L. Li, "High-resolution three-dimensional microwave imaging using a generative adversarial network," in *Proc. Int. Appl. Comput. Electromagn. Soc. Symp. (ACES-China)*, vol. 1. Nanjing, China, 2019, pp. 1–3.
[25] Z. Wei and X. Chen, "Physics-inspired convolutional neural network for solving full-wave inverse scattering problems," *IEEE Trans. Antennas Propag.*, vol. 67, no. 9, pp. 6138–6148, Sep. 2019.
[26] X. Chen, Z. Wei, M. Li, and P. Rocca, "A review of deep learning approaches for inverse scattering problems," *Progr. Electromagn. Res.*, vol. 167, pp. 67–81, Jan. 2020.
[27] I. Bisio *et al.*, "Brain stroke microwave imaging by means of a Newton-conjugate-gradient method in L^p Banach spaces," *IEEE Trans. Microw. Theory Techn.*, vol. 66, no. 8, pp. 3668–3682, Aug. 2018.
[28] I. Bisio *et al.*, "Variable-exponent Lebesgue-space inversion for brain stroke microwave imaging," *IEEE Trans. Microw. Theory Techn.*, vol. 68, no. 5, pp. 1882–1895, May 2020.
[29] K. J. Langenberg, M. Berger, T. Kreutter, K. Mayer, and V. Schmitz, "Synthetic aperture focusing technique signal processing," *NDT Int.*, vol. 19, no. 3, pp. 177–189, Jun. 1986.
[30] K. J. Langenberg, "Linear scalar inverse scattering," in *Scattering: Scattering and Inverse Scattering in Pure and Applied Science*, E. R. Pike and P. C. Sabatier, Eds. San Diego, CA, USA: Academic, 2002, pp. 121–141.
[31] F. Soldovieri and R. Solimene, "Ground penetrating radar subsurface imaging of buried objects," in *Radar Technology*, G. Kouemou, Ed. London, U.K.: IntechOpen, 2010.
[32] R. Potthast, "A study on orthogonality sampling," *Inverse Problems*, vol. 26, no. 7, 2010, Art. no. 074015.
[33] M. T. Bevacqua, T. Isernia, R. Palmeri, M. N. Akinci, and L. Crocco, "Physical insight unveils new imaging capabilities of orthogonality sampling method," *IEEE Trans. Antennas Propag.*, vol. 68, no. 5, pp. 4014–4021, May 2020.
[34] M. T. Bevacqua, R. Palmeri, T. Isernia, and L. Crocco, "Physical interpretation of the orthogonality sampling method," in *Proc. 2nd URSI Atlantic Radio Sci. Meeting (AT-RASC)*, Meloneras, Spain, 2018, pp. 1–3.
[35] C. Estatico, A. Fedeli, M. Pastorino, and A. Randazzo, "Quantitative microwave imaging method in Lebesgue spaces with nonconstant exponents," *IEEE Trans. Antennas Propag.*, vol. 66, no. 12, pp. 7282–7294, Dec. 2018.
[36] C. Estatico, A. Fedeli, M. Pastorino, and A. Randazzo, "Microwave imaging by means of Lebesgue-space inversion: An overview," *Electronics*, vol. 8, no. 9, p. 945, Sep. 2019.
[37] J. W. Massey and A. E. Yilmaz, "AustinMan and AustinWoman: High-fidelity, anatomical voxel models developed from the VHP color images," in *Proc. IEEE 38th Annu. Int. Conf. Eng. Med. Biol. Soc.*, Orlando, FL, USA, 2016, pp. 3346–3349.
[38] M. Fujii, "Maximum frequency range limit of multi-pole Debye models of human body tissues," *IEEE Microw. Wireless Compon. Lett.*, vol. 22, no. 2, pp. 73–75, Feb. 2012.
[39] S. Mustafa, A. M. Abbosh, and P. T. Nguyen, "Modeling human head tissues using fourth-order Debye model in convolution-based three-dimensional finite-difference time-domain," *IEEE Trans. Antennas Propag.*, vol. 62, no. 3, pp. 1354–1361, Mar. 2014.
[40] S.-L. Liew *et al.*, "A large, open source dataset of stroke anatomical brain images and manual lesion segmentations," *Sci. Data*, vol. 5, no. 1, pp. 1–11, Feb. 2018.
[41] C. Warren, A. Giannopoulos, and I. Giannakis, "gprMax: Open source software to simulate electromagnetic wave propagation for ground penetrating radar," *Comput. Phys. Commun.*, vol. 209, pp. 163–170, Dec. 2016.
[42] A. Fedeli, C. Montecucco, and G. L. Gragnani, "Open-source software for electromagnetic scattering simulation: The case of antenna design," *Electronics*, vol. 8, no. 12, p. 1506, Dec. 2019.
[43] P. M. Meaney, C. J. Fox, S. D. Geimer, and K. D. Paulsen, "Electrical characterization of glycerin: Water mixtures: Implications for use as a coupling medium in microwave tomography," *IEEE Trans. Microw. Theory Techn.*, vol. 65, no. 5, pp. 1471–1478, May 2017.

ALESSANDRO FEDELI (Member, IEEE) received the B.Sc. and M.Sc. degrees in electronic engineering and the Ph.D. degree in science and technology for electronic and telecommunications engineering from the University of Genoa, Genoa, Italy, in 2011, 2013, and 2017, respectively, where he is currently an Assistant Professor with the Department of Electrical, Electronic, Telecommunications Engineering, and Naval Architecture. He has coauthored more than 90 scientific contributions published in international journals, conference proceedings, and book chapters. His research activities, carried out with the Applied Electromagnetics Laboratory, are mainly focused on the development and the application of computational methods for the solution of forward and inverse scattering problems, and electromagnetic imaging. He is a member of the IEEE Antennas and Propagation Society, the Italian Society of Electromagnetism, and the Interuniversity Center for the Interaction between Electromagnetic Fields and Biosystems.

CLAUDIO ESTATICO received the Laurea degree in mathematics from the University of Genoa, Genoa, Italy, in 1995, and the Ph.D. degree in computational mathematics and operation research from the University of Milan, Milan, Italy, in 2002. In 2003, he was a participant in the semester program on inverse problems with the Institute for Pure and Applied Mathematics, University of California at Los Angeles, Los Angeles, CA, USA. He is currently an Associate Professor of numerical analysis with the Department of Mathematics, University of Genoa. He has authored or coauthored about 100 journal and conference papers. His research interests are numerical linear algebra and inverse problems. They include regularization in Banach spaces, preconditioning, and iterative methods for linear and nonlinear ill-posed problems, with application in image restoration, inverse scattering, and remote sensing.

MATTEO PASTORINO (Fellow, IEEE) is a Full Professor of Electromagnetic Fields with the University of Genoa, Italy, where he is the Director of the Department of Electrical, Electronic, Telecommunications Engineering and Naval Architecture (DITEN). From 2008 to 2011, he was also the Director of the Department of Biophysical and Electronic Engineering (DIBE). He has authored the book *Microwave Imaging* (Wiley, 2010) and has coauthored the book *Microwave Imaging Methods and Applications* (Artech House, 2018). He has also coauthored more than 450 papers in international journals and conference proceedings. His current research interests include microwave and millimeter-wave imaging, direct and inverse scattering problems, industrial and medical applications, smart antennas, and analytical and numerical methods in electromagnetism. He is currently the Chair of the National URSI Commission B (Fields and Waves), the responsible for the local section of the National Society of Electromagnetics, and the Vice Director of the Interuniversity Center for the Interaction between Electromagnetic Fields and Biosystems. He is a member of the editorial boards and technical program committees of several international journals and conferences in the field of microwaves and antennas. He is currently an Associate Editor of the *IEEE Antennas and Propagation Magazine* and the IEEE OPEN JOURNAL OF ANTENNAS AND PROPAGATION.

ANDREA RANDAZZO (Senior Member, IEEE) received the Laurea degree in telecommunication engineering and the Ph.D. degree in information and communication technologies from the University of Genoa, Italy, in 2001 and 2006, respectively, where he is currently a Full Professor of Electromagnetic Fields with the Department of Electrical, Electronic, Telecommunication Engineering, and Naval Architecture. He has coauthored the book *Microwave Imaging Methods and Applications* (Artech House, 2018) and more than 250 papers published in journals and conference proceedings. His primary research interests are in the field of microwave imaging, inverse scattering techniques, numerical methods for electromagnetic scattering and propagation, and smart antennas.